

Article

Influence of rGO and Preparation Method on the Physicochemical and Photocatalytic Properties of TiO₂/Reduced Graphene Oxide Photocatalysts

Agnieszka Wanag *^{ID}, Ewelina Kusiak-Nejman, Adam Czyżewski, Dariusz Moszyński and Antoni W. Morawski *^{ID}

Department of Inorganic Chemical Technology and Environment Engineering, Faculty of Chemical Technology and Engineering, West Pomeranian University of Technology in Szczecin, Pułaskiego 10, 70-322 Szczecin, Poland; ewelina.kusiak@zut.edu.pl (E.K.-N.); aczyzewsk@zut.edu.pl (A.C.); dariusz.moszynski@zut.edu.pl (D.M.)

* Correspondence: awanag@zut.edu.pl (A.W.); amor@zut.edu.pl (A.W.M.)

Abstract: In this study, a series of TiO₂/rGO photocatalysts were obtained with a two-step procedure: a solvothermal method and calcination at 300–900 °C in an argon atmosphere. It was noted that the presence of rGO in photocatalysts had an important role in the changes in crystallite size and specific surface area. In TiO₂/rGO samples, different surface functional groups, such as C–C_{graph}, C–C_{aliph}, C–OH, C=O, and CO(O), were found. It was observed that rGO modification suppressed the anatase-to-rutile phase transformation. The photocatalytic activity of the obtained nanomaterials was investigated through the decomposition of methylene blue under UV and artificial solar light irradiation. It was found that the adsorption degree played an important role in methylene blue decomposition. The experimental results revealed that TiO₂/rGO samples exhibited superior removal efficiency after calcination for methylene blue compared to TiO₂ without rGO, as well as a commercial photocatalyst KRONOClean 7000. It was noted that photocatalytic activity increased with the increase in the calcination temperature. The highest activity was observed for the sample calcined at 700 °C, which consisted of 76% anatase and 24% rutile. This study clearly demonstrated that TiO₂/rGO samples calcined in argon can be used as efficient photocatalysts for the application of methylene blue decomposition.

Keywords: photocatalysis; TiO₂; reduced graphene oxide; solvothermal and calcination method; adsorption; UV and artificial solar light



Citation: Wanag, A.; Kusiak-Nejman, E.; Czyżewski, A.; Moszyński, D.; Morawski, A.W. Influence of rGO and Preparation Method on the Physicochemical and Photocatalytic Properties of TiO₂/Reduced Graphene Oxide Photocatalysts. *Catalysts* **2021**, *11*, 1333. <https://doi.org/10.3390/catal11111333>

Academic Editor: Christos Trapalis

Received: 3 October 2021

Accepted: 29 October 2021

Published: 2 November 2021

Publisher's Note: MDPI stays neutral with regard to jurisdictional claims in published maps and institutional affiliations.



Copyright: © 2021 by the authors. Licensee MDPI, Basel, Switzerland. This article is an open access article distributed under the terms and conditions of the Creative Commons Attribution (CC BY) license (<https://creativecommons.org/licenses/by/4.0/>).

1. Introduction

Titanium dioxide is commonly used in the photocatalytic process of water purification for the decomposition of different types of organic pollutants, such as heavy metals, pesticides, dyes, and phenols [1,2]. Various modifications of pristine material by metals and non-metal species, or by coupling TiO₂ with other semiconductors, have been conducted to obtain TiO₂ photocatalysts with high photocatalytic activity [3–5]. One of the most promising and widely tested methods of preparation for highly active photocatalysts is modification with carbon due to the enhancement of the photocatalytic activity under visible light irradiation and the suppression of the recombination of the electron–hole pairs [6,7]. Carbon nanomaterials are an interesting group of carbon precursors that can be used in TiO₂ modification due to their unique porous structure, electronic properties, and large adsorptive capacity [8]. Conventional carbon materials, such as carbon black, activated carbon, and graphite, as well as graphitized materials have been widely used in heterogeneous catalysis for many years [9]. Carbon nanomaterials in the form of carbon nanotubes, C60 fullerenes, or graphene provide new possibilities for TiO₂ modification [10]. Graphene especially, as a two-dimensional novel carbon nanomaterial with zero band gap, large specific surface area, and excellent mechanical, electrical, optical, and

thermal properties, has attracted the interest of many researchers [11,12]. Thanks to its unique electronic properties, modification with graphene brings many benefits, such as suppressing electron–hole pair recombination and increasing the specific surface area of tested photocatalysts.

In the literature, several methods of preparation for TiO₂/graphene oxide (TiO₂-GO) and TiO₂/reduced graphene oxide (TiO₂-rGO) photocatalysts have been presented. The most popular methods include simple mixing and/or sonication [13], the sol-gel process [14], and hydrothermal/solvothermal synthesis [15–17]. Other less common methods include electrolytic deposition [18], liquid-phase deposition [19], and synthesis using microwaves [20]. However, the most popular and most commonly used methods are solvothermal and hydrothermal methods. The hydrothermal/solvothermal process can be undertaken in one or two steps. The one-step process typically utilizes previously prepared TiO₂ and graphene materials, while the two-step process involves TiO₂ synthesis from different precursors [21,22]. The hydrothermal solvothermal process is usually undertaken at 120–180 °C for 1–36 h [23–27]. Both methods consist of reactions under controlled temperature and/or using water or organic solvents. Graphene oxide can be reduced during preparation by using these methods if a chemical reagent is added [28]. Additional steps in TiO₂/graphene preparation may be involved. It is well-known that the calcination process significantly improves photocatalytic activity due to the increase in the crystallinity of TiO₂ and the growth of anatase crystallites [29]. However, in the case of TiO₂/graphene photocatalysts, there have only been a few reports of thermal treatment [30–34]. Generally, in these reports, the calcination was carried out in the range of 350–550 °C, probably because of concerns about the oxidation of rGO. Zhang et al. [30] synthesized TiO₂/rGO samples using a hydrothermal method. They used graphene oxide (GO) and TiO₂ from the sol-gel method as starting materials and ethanol-water solution as a solvent. The obtained photocatalysts were calcined at 450 °C for 30 min in an air atmosphere. Obtained samples were characterized by higher photoactivity than the material prepared with the one-step hydrothermal process. The increased photoactivity was attributed to the oxidation of residual organic compounds present in the sample and better crystallization of TiO₂ particles. In contrast, Nguyen-Phan et al. [31] obtained TiO₂/graphene photocatalysts by applying GO paste and TiO₂ P25 and then heating the samples at 200, 400, and 600 °C under an argon atmosphere. The calcined photocatalysts showed higher activity compared to the starting material. However, a decrease in photocatalytic activity with an increase in calcination temperature was observed. It was attributed to the reduction of the surface area and the increase in the size of crystallites.

The motivation to undertake our research was the limited availability of information in the literature about the influence of the calcination step on the physicochemical and photocatalytic properties of TiO₂ modified with rGO, probably because of concerns about oxidation. In our study, we decided to use argon as a calcination atmosphere to circumvent the problem concerning rGO oxidation. Furthermore, our previous study showed that the combination of rGO (1–8 wt.%) modification with calcination at 500 °C may have a substantial impact on the physicochemical properties, as well as photocatalytic activity, of the obtained photocatalysts [35]. In another study [36], it was found that EPR/FMR spectra for TiO₂/rGO samples calcined at 400, 500, and 600 °C showed oxygen defects and a ferromagnetic ordering system connected with trivalent titanium ions. Taking the above into account, we decided to widen the scope of the study and thoroughly examine the impact of these methods on nanomaterial properties. In this work, we focused on a TiO₂ combination with 8 wt.% graphene and calcination at 300–900 °C ($\Delta t = 100$ °C) in an argon atmosphere. It was found that both rGO modification and the calcination process strongly impacted the crystallite size, the changes in the crystal structure, and the specific surface area of the tested samples. The nanomaterials were tested with the photocatalytic decomposition of methylene blue under two types of irradiation: UV and artificial solar light.

2. Results and Discussion

2.1. Characterization of Photocatalysts

2.1.1. UV–Vis Diffuse Absorbance Spectroscopy

In Figure 1, the UV–Vis/DR spectra of TiO₂/rGO-t samples, as well as control and reference KRONOClean 7000 samples, are presented. The TiO₂ material presented typical absorption characteristics for a TiO₂ semiconductor. The sample exhibited high absorption in the UV range and no absorption in the Vis region (above 400 nm). Strong absorption at around 380 nm was noticed, and this was related to the electron transition from the valence band (O 2p) to the conduction band (Ti 3d) [37]. A different situation could be observed for photocatalysts after modification. TiO₂/rGO-t nanomaterials exhibited absorption in the visible region, which increased with the increase in the calcination temperature. The results were related to the colour changes after modification. The highest absorption of visible light was noted for the materials heated at 900 °C with the darkest colour. The dark colour of the sample facilitated visible light absorption [38]. The results showed that the samples calcined at 700, 800, and 900 °C exhibited a significant red-shift in the absorption edge, and this corresponded to the energy band-gap values. The band-gap values of the tested materials are presented in Table 1. The E_g values for TiO₂/rGO-700, TiO₂/rGO-800, and TiO₂/rGO-900 photocatalysts were 3.09, 2.97, and 2.97 eV, respectively. Zhang et al. [39] found that the decrease in the band gap of samples with graphene is related to the formation of the Ti–O–C bond between TiO₂ and the specific sites of carbon. A similar conclusion was proposed by Pastrana-Martínez et al. [40]. In order to confirm the rGO impact on changes in band-gap energy, the values of the E_g for TiO₂ calcined at 700 and 900 °C (without rGO) were examined. The E_g values for these samples were 3.02 and 3.01 eV, respectively, and they were similar to the values for photocatalysts with rGO calcined at 700, 800, and 900 °C. Thus, narrowing of the band gap is mainly caused by calcination in an argon atmosphere rather than the incorporation of carbon from the graphene in the titanium dioxide structure. The red-shift in the adsorption edge and the narrowing of the band-gap energy has also been found to correspond to changes in the TiO₂ phase composition, especially when rutile was present in the tested samples [41,42]. In addition, the intensive absorption peak located at 270 nm was observed for all TiO₂/rGO-t photocatalysts. This peak was attributed to the π - π^* transitions of C=C bonds characteristic for rGO [43,44].

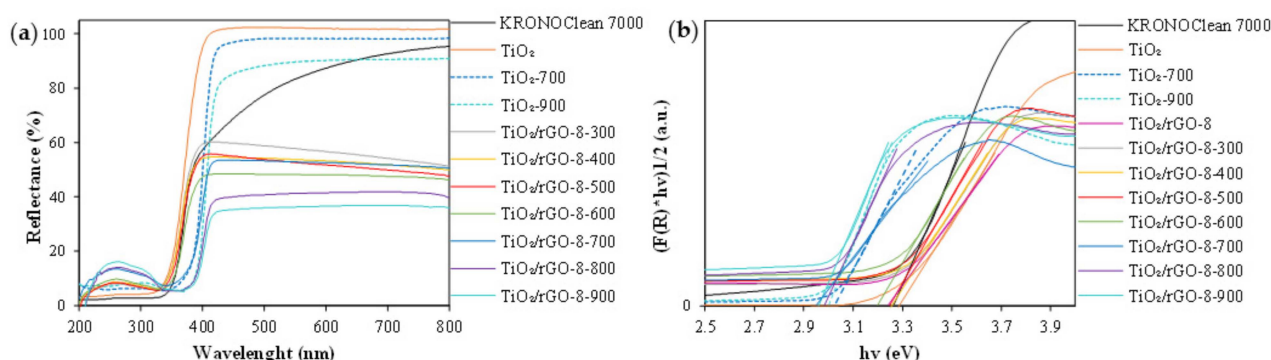


Figure 1. UV–Vis/DR spectra (a) and Tauc plot (b) for reference, control, and obtained photocatalysts.

Table 1. XRD phase compositions and crystallite sizes for reference, control, and obtained photocatalysts.

Sample Code	Crystalline Phase Participation (%)		Anatase		Rutile		E _g (eV)
	Anatase	Rutile	FWHM 2θ = 25.4 (°)	d _A ^a (nm)	FWHM 2θ = 27.7 (°)	d _R ^a (nm)	
KRONOClean 7000	100	0	0.88	11	-	-	3.29
TiO ₂	98	2	0.55	18	0.34	32	3.28
TiO ₂ /rGO	99	1	0.58	17	0.37	27	3.28
TiO ₂ /rGO-300	98	2	0.53	19	0.34	33	3.27
TiO ₂ /rGO-400	98	2	0.53	19	0.32	29	3.28
TiO ₂ /rGO-500	96	3	0.47	22	0.24	93	3.28
TiO ₂ /rGO-600	97	3	0.38	29	0.30	140 *	3.26
TiO ₂ /rGO-700	76	24	0.31	38	0.13	176 *	2.99
TiO ₂ /rGO-800	3	97	0.22	65	0.12	272 *	2.97
TiO ₂ /rGO-900	0	100	-	-	0.12	281 *	2.97
TiO ₂ -300	99	1	0.55	18	0.35	32	3.27
TiO ₂ -500	99	1	0.42	26	0.27	47	3.29
TiO ₂ -700	28	72	0.24	58	0.13	235 *	3.02
TiO ₂ -800	1	99	0.17	105	0.12	338 *	3.01
TiO ₂ -900	0	100	-	-	0.11	423 *	-

^a Mean anatase and rutile crystallite size. * Determination of crystallites above 100 nm was subject to large errors. However, these results are presented for comparative purposes.

2.1.2. X-ray Diffraction Analysis

The XRD patterns of all tested photocatalysts are presented in Figure 2. Photocatalysts obtained at 300–600 °C, as well as the control and reference samples, consisted mainly of anatase phase (up to 98%). This materials exhibited reflection characteristics for the anatase phase—(101), (004), (200), (105), (211), (204), (116), (220), and (215) located at 25.3, 37.6, 47.8, 53.7, 54.8, 62.6, 68.7, 70.2, and 75.0°, respectively (JCPDS 01-070-7348)—and one small reflection characteristic for rutile (110) located at 27.1°. It should be noted that the presence of a low percentage of rutile in materials from the starting TiO₂ was related to the TiO₂ production process, not the phase transformation. In the case of photocatalysts calcined above 600 °C the characteristic reflections for rutile (110), (200), (111), (210), (211), (220), (002), (310), (301), and (112) located at 36.2, 39.8, 41.7, 44.3, 54.8, 56.8, 63.1, 64.7, 69.2, and 69.8° (JCPDS 01-076-0318) were observed. The presence of rutile reflection was related to the anatase-to-rutile phase transformation occurring at a higher temperature. Additionally, it was possible to observe an increase in the intensity of rutile reflection and the gradual disappearance of anatase reflection with the increase in the calcination temperature. A characteristic diffraction peak for reduced graphene oxide located at 24.2° [45] was not found. This was due to the small amount of graphene and its relatively low diffraction intensity, which was possibly shielded by the main peak of anatase TiO₂ (101) located at 25.3° [46]. Similar observations were made by He et al. [47], Yang et al. [48], and other researchers [49,50].

As can be seen in Table 1, the calcination temperature had an important impact on the increase in the crystallite size of both anatase and rutile. The crystallite size increased with increasing calcination temperature. The crystallite sizes of anatase and rutile increased from 17 to 65 nm for anatase and from 27 to more than 100 nm for rutile. This indicated an increase in the crystallinity of the samples after calcination, which was also confirmed by the increase in the intensity of reflection for both anatase and rutile, as shown in Figure 2, and in the decrease in the value of the FWHM parameter for both mentioned phases, as well as the narrower reflections, the larger crystallite size, and the greater degree of crystallinity of the material [51]. As depicted in Figure 2, the anatase-to-rutile phase transformation, in this case, began at 600 °C, where additional reflections of rutile for TiO₂/rGO-8-700 were observed. With the increase of the calcination temperature, the intensity of rutile reflection

also increased. For example, photocatalyst calcined at 900 °C consisted only of rutile. Three reference photocatalysts (TiO₂-700, TiO₂-800, and TiO₂-900) were analyzed to confirm that the modification of graphene contributes to the suppression of phase transition and sintering of TiO₂ particles during temperature modification. Phase composition analysis showed that the TiO₂-700 sample contained 28% anatase and the TiO₂-800 sample only 1% (the content of anatase in the TiO₂/rGO-700 sample was 76% and in the TiO₂/rGO-800 sample it was 3%). It should be pointed out that samples with rGO were characterized by smaller crystallite sizes than the materials without rGO. It can be concluded that the modification with reduced graphene oxide suppressed the phase transition as well as the sintering of TiO₂ crystallites. In the case of the TiO₂-900 sample, no effect of graphene on the phase composition was found. The calcination temperature was too high, so the presence of carbon in the form of rGO suppressed the anatase-to-rutile transformation.

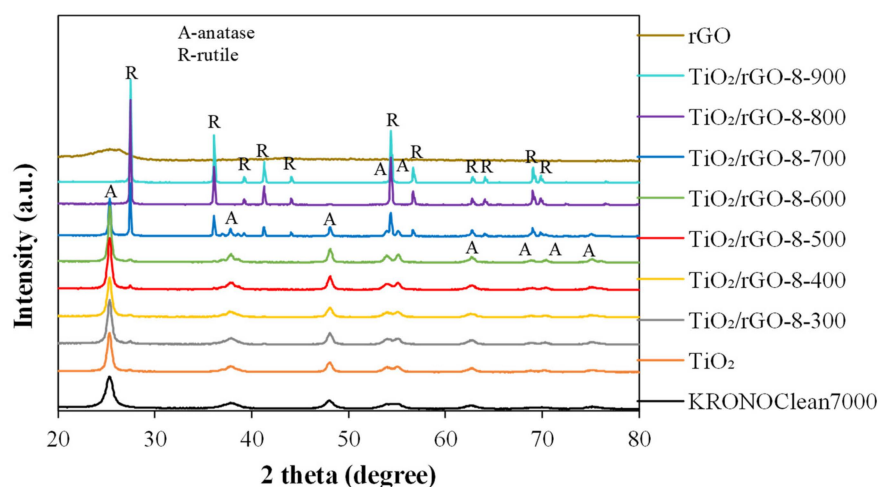


Figure 2. XRD patterns of reference, control, and obtained photocatalysts.

2.1.3. BET Analysis

The S_{BET} values and total pore volume of the tested nanomaterials, as well as the reference materials, are shown in Table 2. The S_{BET} area and total pore volume of the control TiO₂ sample were 97 m²/g and 0.40 cm³/g, respectively. After rGO modification (TiO₂/rGO), the S_{BET} area increased to 142 m²/g, and this was related to using rGO during preparation and its high S_{BET} area (310 m²/g). Kim et al. [26] and Ruidíaz-Martínez et al. [52] also observed an increase of S_{BET} area for samples after hydrothermal modification with rGO. For TiO₂/rGO-*t* photocatalysts obtained with the calcination process, a decrease in the S_{BET} area was observed. It is worth mentioning that the amount of rGO for this group of samples was the same, and it was assumed to be a mass of 8%. S_{BET} area decreased after calcination from 142 m²/g for TiO₂/rGO (starting material for calcination) to 21 m²/g for the sample heated at 900 °C. Furthermore, a correlation between increasing calcination temperature and decreasing surface area was observed. This was related to the sintering and agglomeration of TiO₂ particles during calcination [53,54]. As was previously observed, the modification with graphene led to the increase of the S_{BET} area. The S_{BET} values for TiO₂/rGO-*t* were compared with the values for photocatalysts for TiO₂-*t* materials to verify this phenomenon. It can be observed (see Table 2) that rGO modification caused a suppression of the decrease in S_{BET} values after calcination. For example, the S_{BET} area for TiO₂-700 was 15 m²/g and for TiO₂/rGO-700 it was 58 m²/g. The total pore volume also decreased with the increase in the calcination temperature, and this was a typical phenomenon related to the S_{BET} value decreasing and the increasing crystallite size [7]. However, it was observed that rGO suppression also decreased pore volume. It can be noted that the total pore volume for the TiO₂/rGO-700 samples was almost twice as high as for the sample calcined at the same temperature without rGO, and it was almost five times higher for TiO₂/rGO-700 in comparison to TiO₂-700. It should be concluded that

using rGO for preparation has an important influence on the suppression of the decrease in the S_{BET} and total pore volume.

Table 2. Specific surface area and pore size distribution of studied reference, control, and prepared photocatalysts.

Sample Code	S_{BET} (m^2/g)	$V_{\text{total}}^{\text{a}}$ (cm^3/g)	$V_{\text{micro}}^{\text{b}}$ (cm^3/g)	$V_{\text{meso}}^{\text{c}}$ (cm^3/g)	Carbon Content (wt%)
KRONOClean 7000	249	0.37	0.09	0.28	0.96
TiO ₂	97	0.40	0.04	0.36	0.6
TiO ₂ /rGO	142	0.42	0.04	0.38	6.5
TiO ₂ /rGO-300	134	0.44	0.04	0.40	5.8
TiO ₂ /rGO-400	117	0.35	0.04	0.31	5.9
TiO ₂ /rGO-500	114	0.41	0.04	0.37	5.9
TiO ₂ /rGO-600	63	0.75	0.03	0.72	6.0
TiO ₂ /rGO-700	58	0.24	0.02	0.22	5.7
TiO ₂ /rGO-800	23	0.08	0.01	0.07	5.9
TiO ₂ /rGO-900	21	0.04	0.01	0.03	5.4
TiO ₂ -300	112	0.30	0.04	0.26	-
TiO ₂ -500	78	0.23	0.03	0.20	-
TiO ₂ -700	15	0.05	0.004	0.046	-
TiO ₂ -900	4	0.04	0.01	0.03	-
rGO	310	0.32	0.12	0.20	75

^a Total pore volume determined by the signal-point nitrogen adsorption isotherms at relative pressures $p/p_0 = 0.989$. ^b Micropore volume estimated using the Dubinin–Radushkevich method. ^c Mesopore volume determined as the difference between V_{total} and V_{micro} .

The influence of reduced graphene oxide on the structural properties of rGO-decorated TiO₂ photocatalysts was also confirmed by studying the character of the adsorption–desorption isotherms presented in Figure 3. Based on the IUPAC classification, the isotherms of the tested photocatalysts exhibited characteristics of the type IV rank [55] attributed to mesoporous-like materials. Only the TiO₂-700 sample demonstrated type II isotherm characteristics, associated with non-porous materials, for which the hysteresis loop does not appear. All tested photocatalysts presented the same H3-type hysteresis loop [56]. However, in the case of the samples with rGO, the value of the adsorbed N₂ rapidly increased, and the hysteresis loop between the adsorption and desorption branches of the isotherm was wide. This type of enlargement of hysteresis, in the range of 0.45–0.7, is related to rGO content [57].

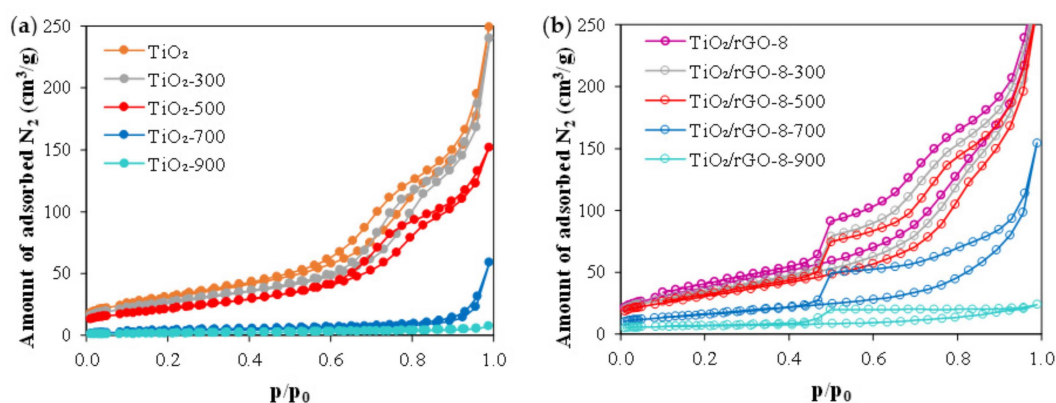


Figure 3. Adsorption–desorption isotherms for (a) reference, control, and (b) obtained photocatalysts.

2.1.4. SEM Image Analysis

The presence of graphene flakes in the tested materials was proved by means of SEM microscopy. The SEM image in Figure 4a shows that the rGO sheet was wrinkled,

transparent, and thin. The rGO surface was not covered by adsorbed contaminants. It can be noted that the rGO consisted of 2–4 layers according to the information given by the manufacturer [58]. Sample TiO_2 , shown in Figure 4b, consisted of particles that aggregated into a larger form. The grains presented a regular round shape. After calcination, a decrease in agglomerate size was observed (Figure 4c). Furthermore, the crystallites in TiO_2/rGO -500 exhibited a more spherical shape. TiO_2 nanoparticles were supported on the rGO sheets. Based on Figure 4c, it can also be concluded that a high calcination temperature does not cause any destruction in rGO sheets.

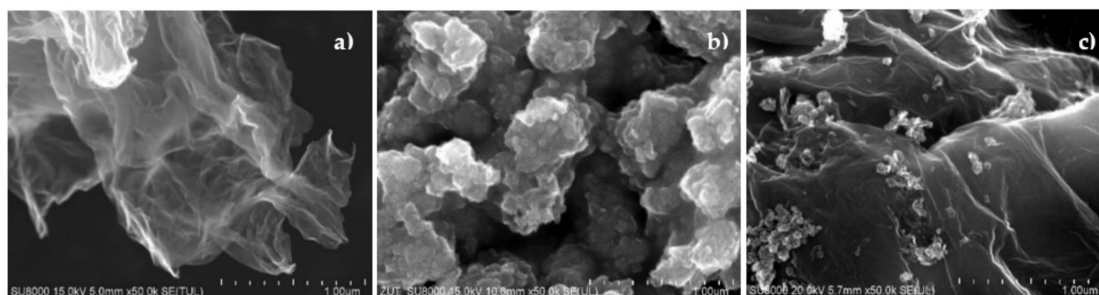


Figure 4. SEM images of (a) rGO, (b) TiO_2 , and (c) TiO_2/rGO -8-300.

2.1.5. Raman Analysis

Raman spectroscopy was used as an additional means of confirmation of the presence of rGO in the TiO_2 sample. Exemplary Raman spectra of TiO_2/rGO -t samples calcined at 300, 500, and 700 °C, as well as the control and reference photocatalysts, are shown in Figure 5. For all analyzed samples, the characteristic bands corresponding to the $E_{g(1)}$, $B_{1g(1)}$, $A_{1g}+B_{1g(2)}$, and $E_{g(2)}$ modes of anatase located at 146, 395, 513, and 636 cm^{-1} were found [59]. The E_g band located at 448 cm^{-1} [60] characteristic of rutile was observed only for the TiO_2/rGO -700 photocatalyst. However, it should be noted that rutile was also present in samples obtained at 800 and 900 °C, as was confirmed by XRD analysis. Due to the low rutile content present in the Raman spectra of the other samples, the characteristic bands are not indexed. Two characteristic peaks at about 1296 cm^{-1} and 1611 cm^{-1} attributed to the D and G bands of the graphitized structure were noted for samples modified with rGO. The D band (disordered) was attributed to the edge or in-plane sp^3 defect of carbon. The presence of this band provides information about defects, and it indicates internal structural defects, dangling bonds, and edge defects [61,62]. The G band (graphitic) was assigned to in-plane stretching vibrations of the symmetric sp^2 C–C bonds, and it was indicated by the degree of organization of the aromatic structure [63]. These two types of bands confirmed the presence of reduced graphene oxide in the TiO_2/rGO -t nanocomposites. In addition, the high-intensity ratio of D and G bands ($I_D/I_G = 1.5$) was attributed to the presence of smaller but more numerous sp^2 domains in the carbon [64]. No characteristic peak corresponding to carbon was observed in the cases of TiO_2 and KRONOClean 7000, despite carbon analysis confirming its presence in the samples (see Table 2). This was due to the presence of another kind of carbon group. The TiO_2 photocatalyst contained alkyl groups from isopropanol, and KRONOClean 7000 had arylcarboxylate groups characteristic of the production process.

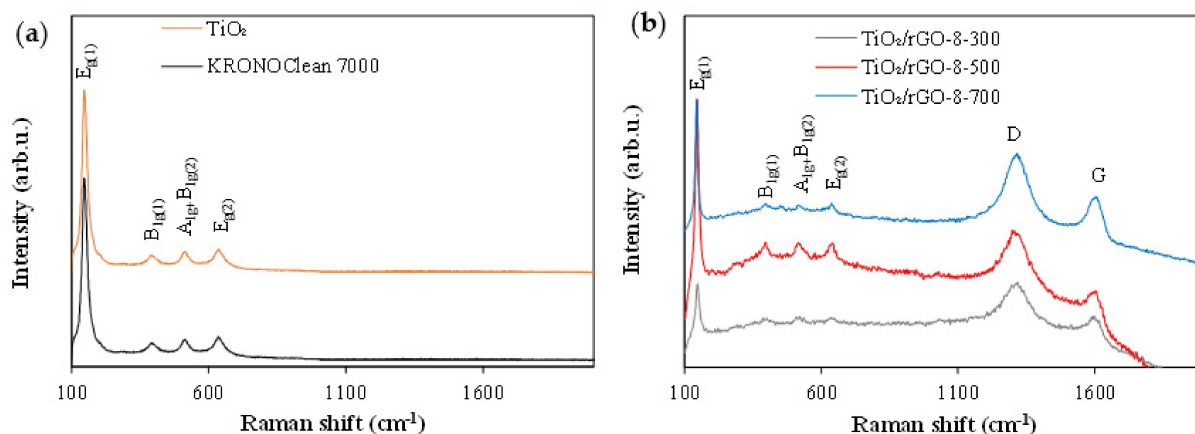


Figure 5. Raman spectra of (a) reference, control, and (b) exemplary obtained photocatalysts.

2.1.6. Thermal Analysis

The TG and DTG curves of the rGO, TiO₂, and TiO₂/rGO photocatalysts are shown in Figure 6. The TG/DTG curves of the rGO and modified TiO₂ samples were characterized by the presence of three distinct mass-loss stages. The first stage, located in the temperature range between ca. 20 and 150 °C (region A), was attributed to the vaporization of water and organic solvent (isopropanol) from the surfaces of the materials. The second mass-loss stage, located between ca. 150–400 °C (region B), was connected with the occurrence of two separate effects, characteristic of the respective materials. Thus, for the rGO material, the mass decline was associated with the decomposition of more labile groups (carboxylate and hydroxylate) and the removal of oxygen molecules [65]. In addition, and in contrast to the rGO material, the TiO₂ sample was characterized by a noticeable mass decline located in region C (between ca. 400–600 °C). This change was attributed to the transformation of the amorphous part of the TiO₂ into the crystalline phase [66,67]. It should also be noted that, above 600 °C (region D), the TG profile of the rGO material gradually declined, indicating the occurrence of high-temperature pyrolysis in the carbon skeleton [24].

Further TG/DTG profiles, presented in Figure 6a,b, were obtained for the exemplary TiO₂/rGO composites calcined at 300, 500, 700, and 900 °C. The shapes of the profiles were clearly dependent on the calcination conditions applied during the material preparation process. Similarly, as in the case of the precursor materials, the TiO₂/rGO-300 and TiO₂/rGO-500 composites exhibited significant mass loss in region A, resulting from the vaporization of residual water and solvent molecules from the material surface. The samples also demonstrated noticeable mass drops in temperature regions B and D, which were ascribed to the thermal decomposition of more labile groups of the rGO component and the degradation of its carbon skeleton, respectively. Furthermore, for the TiO₂/rGO-300 material, an additional mass loss was recorded between ca. 450–600 °C (region C). This change was ascribed to the occurrence of the heat-induced amorphous TiO₂ crystallization process, which was also observed in the case of the TiO₂ precursor sample. In contrast to the previously described counterparts, the remaining TiO₂/rGO-700 and TiO₂/rGO-900 composites exhibited higher thermal stability, which was reflected by the relatively stable progression of the TG curves and negligible weight loss of the materials. This trait was connected with the high-temperature heat treatment applied during the composite preparation process.

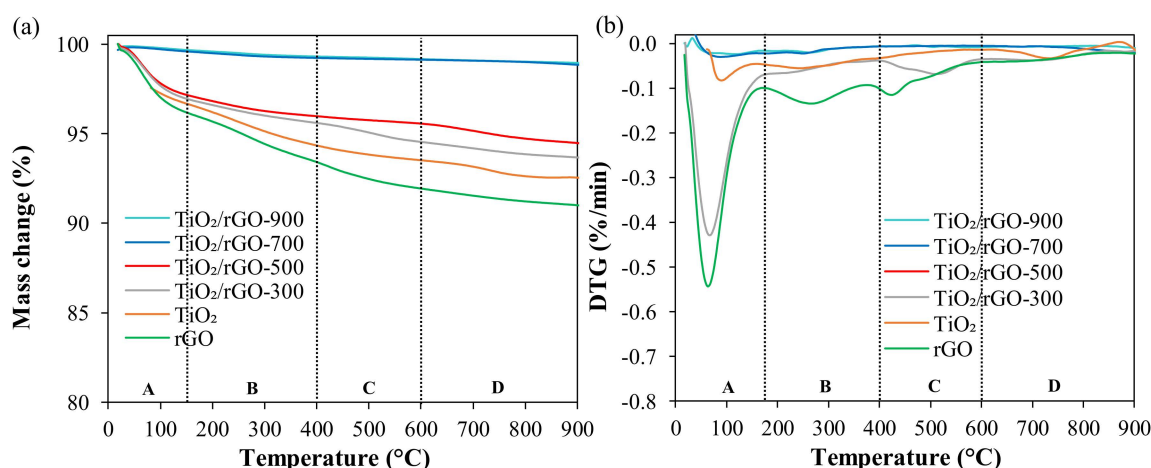


Figure 6. TG (a) and DTG (b) curves for control and obtained photocatalysts.

2.1.7. XPS Analysis

Further detailed characterization of the chemical composition of the $\text{TiO}_2/\text{rGO}-t$ samples calcined at 300, 500, 700, and 900 °C was provided by X-ray photoelectron spectroscopy. High-resolution spectra were acquired to evaluate the chemical states of the elements present on the surfaces of the samples. Only titanium, oxygen, and carbon atoms were identified in all these materials. In Figure 7, a binding-energy region characteristic for Ti 2p transition is depicted for the sample $\text{TiO}_2/\text{rGO}-900$. Two peaks centered at 458.8 eV and 464.6 eV were noted, which corresponded to the Ti 2p_{3/2} and Ti 2p_{1/2} spin-orbit splitting photoelectrons in the Ti⁴⁺ state [68]. There were no differences for the location and shape of the XPS Ti 2p spectra originating from any of the $\text{TiO}_2/\text{rGO}-t$ samples. The position of the main maximum at a binding energy of 458.8 eV proved that titanium atoms were not involved in any kind of strong bond apart from the Ti–O bonds characteristic of TiO_2 . The results indicate that the chemical state of titanium atoms is not influenced by calcination at high temperatures.

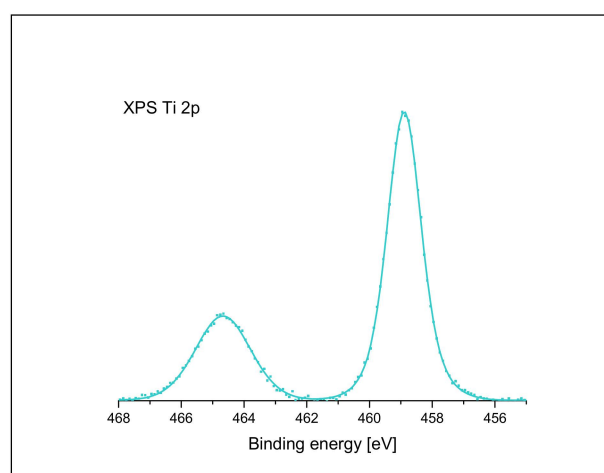


Figure 7. X-ray photoelectron spectrum of Ti 2p transition for $\text{TiO}_2/\text{rGO}-8-900$ sample.

Much more significant changes were observed in the XPS spectra obtained for the considered samples in the C 1s region (see Figure 8). A spectrum acquired for the rGO used for the preparation of hybrid materials was taken as a reference (the gray area). The maximum of the reference spectrum was located at the binding energy of 284.3 eV, a value characteristic of graphene and other graphite-like structures. The maxima of the $\text{TiO}_2/\text{rGO}-t$ samples were generally located at identical positions as in the rGO spectrum.

The observed variations were within the experimental error (0.1 eV). The envelope of the XPS C 1s spectra obtained for the samples calcined at 300, 500, and 700 °C notably differed from the C 1s spectrum of reduced graphene oxide. The most prominent deviations were observed in two regions at about 286 eV and 289 eV. The former region is usually ascribed to the presence of C–O bonds, as in alcohols or ethers. The latter region is typical of carbon–oxygen bonds, where the carbon atom is accompanied by at least two oxygen atoms. Representative examples of such a chemical environment include carboxyl and carboalcoxy functional groups. The surfaces of the TiO₂/rGO-t samples calcined at 300, 500, and 700 °C were abundant in carbon–oxygen bonds of different kinds.

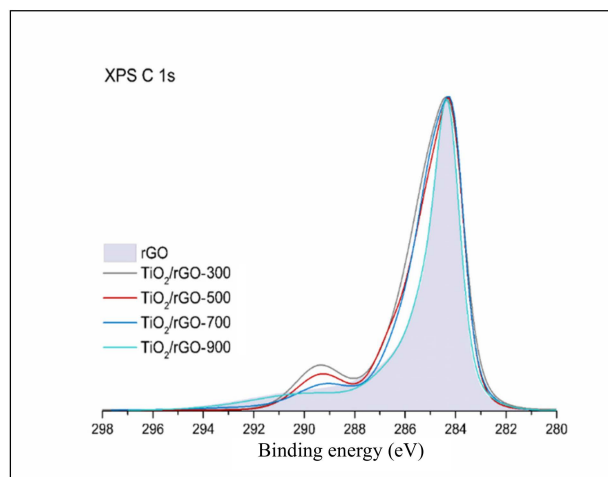


Figure 8. X-ray photoelectron spectra of C 1s transition for reduced graphene oxide (rGO) and selected TiO₂ and rGO hybrid materials.

To address this problem numerically, the deconvolution of the experimental data was undertaken by applying a model consisting of six basic components of C 1s transition. The first component, C–C_{graph}, with a binding energy of 284.3 ± 0.1 eV, essentially corresponded to non-functionalized carbon atoms located in graphene rings. The second component, C–C_{aliph}, with a binding energy of 285.3 ± 0.2 eV, was attributed to sp³ carbon atoms, bonded with either second carbon atoms or hydrogen atoms. Component C–OH, which shifted 2.2 ± 0.2 eV from component C–C_{graph} in the direction of increasing binding energies, was ascribed to a group of carbon atoms linked to one atom of oxygen. The group comprised the following functional groups, which were presumably present in the studied materials: C–O–C and C–OH. The carbon denoted by the asterisk in the *C–O–C=O group could also have contributed to the signal of the component C–OH. The component C=O, which shifted 3.2 ± 0.2 eV from the first component in the direction of increasing binding energies, also corresponded to a set of functional groups: C=O or O–C–O. The fifth component, CO(O), which shifted 5.0 ± 0.2 eV from the component C_{graph}, corresponded to a set of functional groups similar to carboxyl or carboalcoxy. The sixth peak in the C 1s spectra was a shake-up structure caused by the $\pi \rightarrow \pi^*$ -transition in the graphite rings. The binding energy assignments described above are based on the energy shifts given in Appendix E of [69]. The results of the numerical deconvolution are shown in Table 3 and indicated a relative surface functional group composition. The total C 1s intensity was taken as 100. The comparison of the results for the samples calcined at different temperatures shown in Table 3 indicated relatively small variations for components C–C_{graph}, C–C_{aliph}, and C–OH. In general, the component C–C_{aliph} was more prominent on the surfaces of the samples calcined at 300, 500, and 700 °C. It was ascribed to the presence of the isopropanol used during the preparation stage. The most crucial changes were observed for component CO(O), which was in accordance with the component C=O. About 11% of the surfaces of the samples TiO₂/rGO-300 and TiO₂/rGO-500 contained this component, which was observed as an intense local maximum at 289 eV. This component

diminished with increasing calcination temperature and at 900 °C it was negligible. The surface of the sample calcined at 900 °C contained even fewer C–O bindings than observed for pure rGO.

Table 3. The relative surface functional group composition of the total C 1s signal.

Sample Code	C 1s Components (Total C 1s Intensity = 100)					
	C–C _{graph}	C–C _{aliph}	C–OH	C=O	CO(O)	$\pi \rightarrow \pi^*$
rGO	57	21	8	4	4	6
TiO ₂ /rGO-300	54	26	6	3	11	-
TiO ₂ /rGO-500	53	27	7	2	11	-
TiO ₂ /rGO-700	56	29	7	1	7	-
TiO ₂ /rGO-900	60	21	7	3	2	7

2.1.8. Carbon Content

The carbon content in the TiO₂/rGO-t samples is presented in Table 2. For comparison, carbon amounts in the TiO₂, TiO₂/rGO, and reference KRONOClean 7000 photocatalysts are also shown. According to the listed results, the commercial carbon-modified photocatalyst contained 0.96 wt.% carbon. The TiO₂ control sample obtained according to the procedure for modification of TiO₂/rGO-t photocatalysts but without the addition of rGO contained 0.6 wt.% carbon. The presence of carbon in this sample was related to the use of isopropanol in the modification process. It is worth mentioning that the starting TiO₂ did not contain any carbon. TiO₂/rGO, which was a starting material for the calcination process, contained 6.5 wt.% carbon, and this result was different from the theoretically assumed carbon amount used during the modification (8 wt.%). This difference was related to the type of graphene precursor used. The reduced graphene oxide used for modification contained approximately 75 wt.% carbon. Thus, the graphene used was in a form that was not entirely reduced and it had various types of functional groups on its surface (see Section 2.1.7). After the calcination process, the photocatalysts contained almost the same amounts of carbon (about 6 wt.%). However, it was possible to observe differences in the carbon content between TiO₂/rGO and the samples after calcination, and these were related to the evaporation of the residual isopropyl alcohol used in the modification during the first step involving a pressure autoclave.

2.2. Adsorption Experiment

The adsorption properties and the time required to achieve the adsorption–desorption equilibrium between photocatalysts, surface, and contaminant were determined. In Figure 9, the adsorption of MB on the tested nanomaterials under dark conditions is presented. The adsorption–desorption equilibrium was achieved after 180 min. The adsorption degrees calculated for TiO₂ and KRONOClean 7000 were negligible (1.49% and 2.44%, respectively). In contrast, the adsorption degree for the TiO₂/rGO-t nanomaterials was approximately 50%. It is well-known that adsorption properties are related to high S_{BET} values and porous structure. It should be noted that, in spite of decreasing S_{BET} area after calcination, the adsorption properties remained at the same level for all photocatalysts. This was caused by strong π - π interactions between the dye molecules and aromatic regions of reduced graphene oxide [70]. It is also widely known that a negatively charged semiconductor surface has a higher potential for contact with positively charged MB molecules due to the electrostatic attractive interactions [71,72]. The zeta potential for KRONOClean 7000 was +20.64 mV, for TiO₂ it was +12.41 mV, and for TiO₂/rGO-8-800 it was –18.80 mV; thus, in this case, changing the surface charge of TiO₂ from positive to negative after heating caused increases in the adsorption properties of the TiO₂/rGO samples.

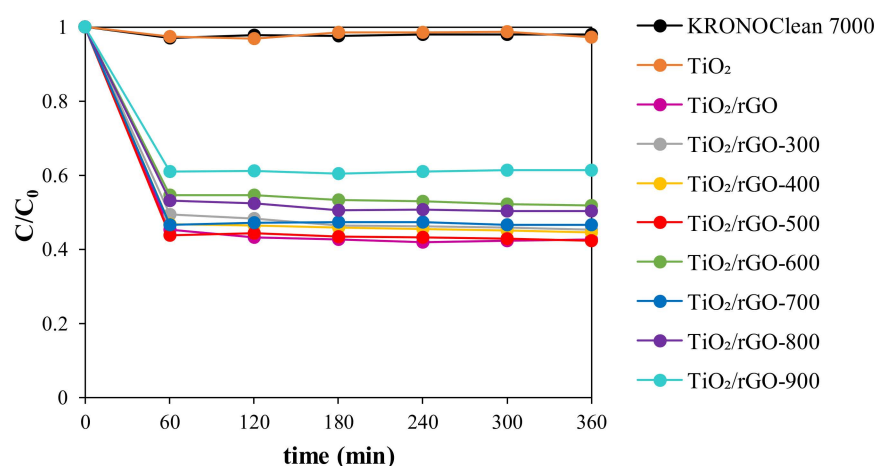


Figure 9. Methylene blue adsorption on the surfaces of reference, control, and prepared photocatalysts.

2.3. Photocatalytic Activity Test

The photoactivity of the TiO_2 and rGO-modified samples in comparison with the commercial photocatalyst KRONOClean 7000 was determined on the basis of the degradation of MB under UV and artificial solar light irradiation. Figure 10 presents the efficiencies of all tested photocatalysts in methylene blue degradation under both types of irradiation. Generally, $\text{TiO}_2/\text{rGO}-t$ nanomaterials showed higher photoactivity in comparison with control and reference samples. The photocatalytic activity of TiO_2 and KRONO-Clean 7000 was negligible, indicating that these samples do not act as effective photocatalysts. Complete MB removal for these samples was achieved after 360 min of irradiation under UV light. In the case of ASL, the decomposition degree was not more than 5%. In contrast, series composites after rGO modification exhibited clearly higher photocatalytic activity under both types of irradiation. It could easily be seen that the activity under UV irradiation increased with the increase of the heat treatment temperature up to 700 °C. This type of correlation was not observed in the case of degradation under artificial solar light. However, in both cases $\text{TiO}_2/\text{rGO}-700$ nanomaterial had the highest photoactivity, with 100% MB decomposition in 90 min of UV irradiation and 31.3% MB decomposition in 300 min of ASL irradiation. It should be noted that adsorption did not have a significant effect on the improvement of activity in the rGO modified samples. Calcination temperature played a prominent role. To better visualize the impact of rGO modification on photoactivity, the results for $\text{TiO}_2/\text{rGO}-700$ and TiO_2-700 are presented in Table 4. The photocatalyst with rGO showed higher activity than the sample obtained through the same procedure without rGO. Several parameters, such as S_{BET} area, crystal structure, and crystallite size, should be taken into account to explain this phenomenon. First of all, the $\text{TiO}_2/\text{rGO}-700$ had a higher S_{BET} area (58 m^2/g) than the TiO_2-700 sample (15 m^2/g). It is well-known that large surface area and phase content have an important influence on the improvement of photocatalytic efficiency. The large surface area provides a number of active sites which can adsorb a large number of contaminant particles [29,73]. Samples containing more anatase than rutile generally exhibit higher activity, as shown in Figure 10. It is widely known that rutile is a less active phase of TiO_2 than anatase due to the lower numbers of active sites and hydroxyl groups on the surface [74]. However, it is worth taking note of the relatively high activity under artificial solar light for the photocatalysts obtained at 800 and 900 °C, which consisted mainly of rutile phase. $\text{TiO}_2/\text{rGO}-800$ and $\text{TiO}_2/\text{rGO}-900$ nanomaterials showed higher activity than the samples modified at temperatures lower than 700 °C. In these cases, the higher photoactivity was related to the redshift edging toward visible light and the narrowing of the band-gap energy. Previous work has suggested that the best proportion between anatase and rutile phases is 75–85% anatase and 15–25% rutile, as in the case of the most popular commercial photocatalyst AEROXIDE[®] TiO_2 P25. It has been stated that such proportions for the anatase-to-rutile ratio are desirable due to

the better separation of charge carriers and higher activity [75,76]. A similar trend was observed for the TiO₂/rGO-700 sample, which contained 85% anatase and 15% rutile and showed the highest photoactivity under both UV and ASL irradiation. The photoactivity also depends on the degree of crystallinity and the crystallite size: the better the crystallized material, the higher the photoactivity [77]. Thus, the samples with lower FWHM parameters demonstrated higher activity. With higher calcination temperatures, the FWHM parameter was lower and the crystallinity greater. Zhang et al. [30] found that the higher efficiency of samples modified with graphene and calcined was related to an increase in crystallinity. It is well-known that the optimal crystallinity size for better efficiency is 10 nm [78]. However, Almquist and Biswas [79] determined that photoefficiency is the highest when the crystallite size is between 25 and 40 nm, which is in concordance with our observations. In our case, the highest activity was associated with samples with crystallite sizes up to 47 nm.

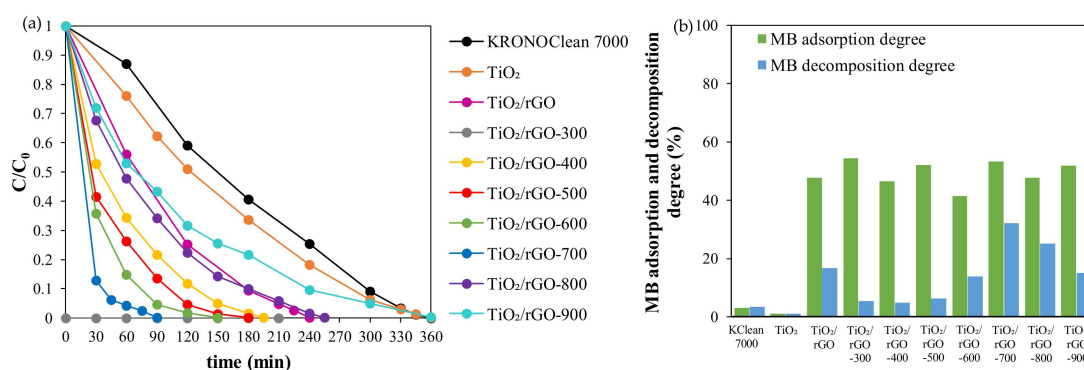


Figure 10. Degree of methylene blue decomposition under (a) UV light and (b) artificial solar light.

Table 4. Degree of methylene blue adsorption and decomposition.

Sample Code	UV Irradiation		Artificial Solar Light	
	Degree of Adsorption (%)	Degree of MB Decomposition after 90 min (%)	Degree of Adsorption (%)	Degree of MB Decomposition after 300 min (%)
KRONOClean 7000	2.1	29.14	3.01	3.36
TiO ₂	2.9	38.78	1.11	1.02
TiO ₂ /rGO-700	62.29	100.00	53.37	32.13
TiO ₂ -700	11.78	86.48	9.24	7.11

2.4. Photocatalyst Stability

The photoactivity of nanomaterials is an essential parameter from a practical application point of view. As it had the highest photoactivity, the TiO₂/rGO-700 photocatalyst was used as the representative sample to examine the long-term stability under UV light irradiation. The results are presented in Figure 11. A slight decrease in activity after the first cycle was observed. It could have been caused by the blocking of active sites on the photocatalyst surface due to the adsorption dye molecules. Janus et al. suggested that carbon deposits from dye degradation can easily be deposited on the surface of tested material [80]. In the case of the TiO₂/rGO-700, a change in the color of the photocatalyst to gray-blue indicated the presence of carbon deposits. However, the degree of activity was at the same level up to the third cycle. A decrease in the photoactivity was noted only after the seventh cycle, related to the distribution of carbon deposits adsorbed on the photocatalyst surface. The decomposition of the byproducts of the MB decomposition is a competitive process for the photoremoval of the main contaminant. The presented

results indicate that the obtained sample exhibited relatively high stability during the photocatalytic decomposition.

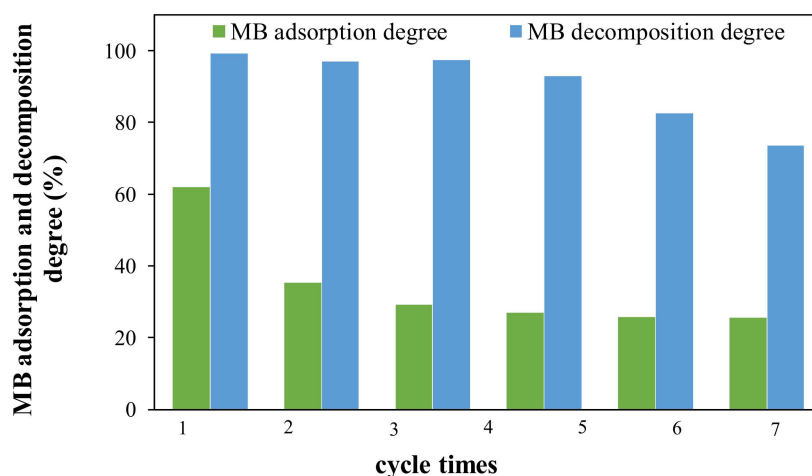


Figure 11. Cycling stability of adsorption and decomposition of methylene blue for the TiO₂/rGO-8-700 sample under UV light.

2.5. Photocatalytic Mechanism

The possible photocatalytic mechanism of TiO₂/rGO nanomaterials is proposed in Figure 12. As a photon with energy higher than the band-gap energy of the semiconductor becomes adsorbed by the photocatalyst, electrons are excited and move from the valance band (VB) to the conduction band (CB), forming a hole. Generally, the generated charges recombine quickly and only a small fraction take part in the photodegradation of the pollutant, resulting in low photocatalytic efficiency. However, in the case of TiO₂ modified with rGO, the electron–hole pair path is different. Due to excellent electronic conductivity, the formed electron is transferred to the graphene sheets, and the charges are well-separated. Thus electron–hole pair recombination is suppressed, and the photoactivity is highly improved. Then, photogenerated electrons react with dissolved oxygen molecules, forming superoxide radical anions (O₂^{•−}), which directly degrade the MB. Eventually, the holes from the CB can react with the water molecule to create hydroxyl radicals (•OH) and destroy MB. Another way is through direct decomposition of the reaction between the holes and MB molecules. In the case of ASL irradiation, the MB molecules also act as sensitizers and self-degradation can take place [81]. It is worth mentioning that adsorption also plays a significant role in photocatalytic mechanisms. Due to the high specific surface area of rGO and the strong π - π interaction between the dye molecules and aromatic regions of the reduced graphene oxide, the pollutants' adsorption is enhanced. Taking this into account, the combination of TiO₂ with rGO can effectively improve the adsorption of MB, as well as the charge transfer reaction [52].

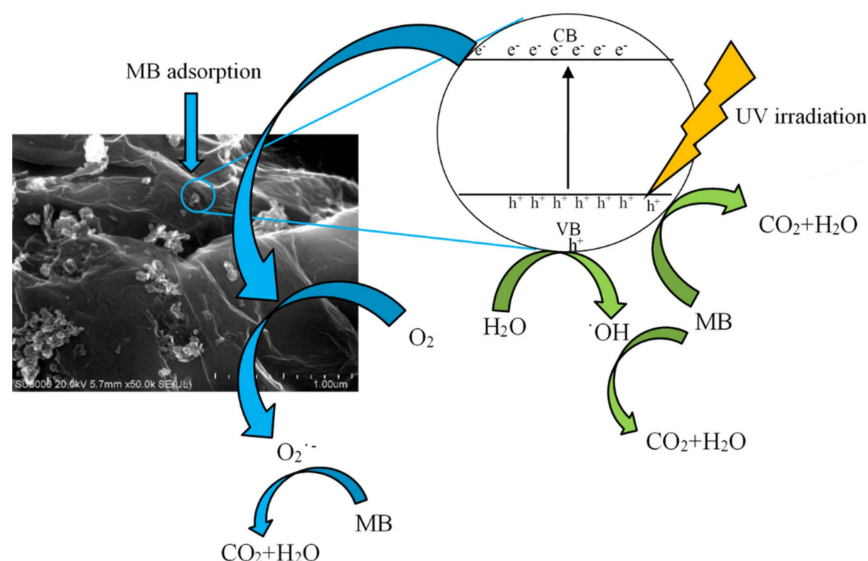


Figure 12. The reaction mechanism for photocatalytic degradation of MB with TiO₂/rGO photocatalyst under UV irradiation.

3. Materials and Methods

3.1. Materials

Crude titanium dioxide supplied by Chemical Plant Grupa Azoty Zakłady Chemiczne “Police” S.A. (Poland) was used as a material for preparing photocatalysts. Taking into account the fact that the product contained 2.1 wt.% residual sulfur (from post-production sulfuric acid), pre-treatment was necessary. The pre-treatment process has been described in detail elsewhere [82]. The TiO₂ used for modification was denoted as starting TiO₂. Reduced graphene oxide prepared with a modified Hummer’s method was supplied by Nanomaterials LS (Poland). The isopropanol (pure p.a. 99.5%) used during the solvothermal treatment was purchased from Firma Chempur (Poland). The commercial photocatalyst KRONOClean 7000 (Kronos Worldwide, Inc., USA) was used as a reference carbon-modified titania nanomaterial. Ultrapure water from a Millipore Elix Advantage water purification system (Merck KGaA, Germany) with a conductivity of 0.04 μS/cm at 25 °C was used for experiments.

3.2. Preparation of Photocatalysts

TiO₂/reduced graphene oxide (TiO₂/rGO) photocatalysts were obtained in two steps: a solvothermal process and calcination. In the first step, 2 g of starting TiO₂ with 8 wt.% reduced graphene oxide were mechanically mixed in a mortar and placed in a pressure reactor with 2 mL of isopropanol. The sample was modified at 180 °C for 4 h under autogenous pressure. Then, the valve in the reactor was opened, and the material was heated for 1 h without pressure to remove residual alcohol and water. Next, the reactor was cooled down to room temperature. The obtained nanomaterial was named TiO₂/rGO-8 and was used as a control material. In the next step, the TiO₂/rGO sample was calcined in an argon atmosphere (purity: 5.0, Messer Polska Sp. z o.o., Chorzów, Poland) in the temperature range of 300–900 °C (Δt = 100 °C) for 4 h in an Ar flow (60 mL/min). The heat treatment process was conducted in a GHC 12/900 horizontal furnace (Carbolite Gero Ltd, Sheffield, UK). Before the heating step, the argon was passed through the quartz tube for 30 min to remove the air present in the quartz tube. The obtained products were named TiO₂/rGO-*t*, where *t* indicates the temperature of calcination. The other TiO₂ control sample was received similarly but without the addition of reduced graphene oxide. The TiO₂ sample was calcined under the same conditions as the photocatalysts with rGO (the samples were named TiO₂-*t*, where *t* indicates the temperature of calcination) in order to examine the influence of rGO modification.

3.3. Characterization of Photocatalysts

The crystalline phase and crystal structure were analyzed by XRD analysis (Malvern PANalytical Ltd., Almelo, The Netherlands) using Cu K α radiation ($\lambda = 1.54056 \text{ \AA}$). The anatase and rutile amounts and the average crystallite size of anatase were calculated using the method described elsewhere [35]. The surface morphologies were observed using scanning electron microscopy (SU8020 Ultra-High Resolution Field Emission Scanning Electron Microscope; Hitachi Ltd., Japan). The Brunauer–Emmett–Teller (BET) surface area and pore size distribution were determined according to the N₂ adsorption–desorption at $-196 \text{ }^\circ\text{C}$ with a Quadrasorb evoTM Gas Sorption analyzer (Anton Paar GmbH, Graz, Austria; previously Quantachrome Instruments, USA). Prior to adsorption measurement, all samples were degassed at $100 \text{ }^\circ\text{C}$ under a high vacuum for 12 h in order to remove residual water and organic carbon residues adsorbed on the surfaces of the tested samples. The carbon content in the studied photocatalysts was calculated using a CN628 LECO elemental analyzer (LECO Corporation, St. Joseph, MI, USA). The certified EDTA standard (LECO Corporation, USA) containing 41.06 and 9.56 wt.% of carbon and nitrogen, respectively, was used for the preparation of a calibration curve. Raman spectra were recorded using an inVia Raman Microscope (Renishaw PLC, New Mills, Wotton-under-Edge, UK) with an excitation wavelength of 785 nm. The diffuse-reflectance UV–Vis spectra were recorded with a V-650 UV–Vis spectrophotometer (JASCO International Co., LTD., Tokyo, Japan) equipped with an integrating sphere accessory for studying DRS spectra. Barium sulfate was used as the reference material. The X-ray photoelectron spectroscopy (XPS) experiments were performed using Al K α ($h\nu = 1486.6 \text{ eV}$) radiation with a Scienta SES 2002 spectrometer (Scienta Scientific AB, Uppsala, Sweden) operating at constant transmission energy ($E_p = 50 \text{ eV}$). The thermal stability of the obtained photocatalysts was investigated using thermogravimetric analysis (TGA). The thermal stability of the tested photocatalysts was investigated with a NETZSCH STA 449 C (NETZSCH-Gerätebau GmbH, Germany) TGA analyzer. A sample (ca. 10 mg) of the tested material was placed in an alumina crucible and heated in an inert (nitrogen) atmosphere up to $900 \text{ }^\circ\text{C}$ with a heating rate of $10 \text{ }^\circ\text{C}/\text{min}$.

3.4. Adsorption Experiment

The adsorption abilities of all studied materials were examined to determine the adsorption properties of the samples and the moment of the liquid–solid equilibrium. The investigation was undertaken using methylene blue as a model organic contaminant. The experiment was carried out in a glass beaker (0.3 L) containing 0.8 g/L of photocatalyst and 0.2 L of contaminant aqueous solution. The starting concentration of the dye was 10 mg/L. The suspension was magnetically stirred without light until the adsorption equilibrium was established. During the experiment, the suspension solutions were centrifuged every 60 min to remove the TiO₂ nanoparticles. The concentration of methylene blue in the solutions was measured using a UV–Vis V-630 spectrophotometer (JASCO International Co., LTD., Tokyo, Japan).

3.5. Photocatalytic Activity Measurements

The photocatalytic activity of the tested nanomaterials was determined according to the degradation process of methylene blue, which was used as a model organic water contaminant. It is remarkable that, although MB tends to absorb light itself, in this case self-degradation was negligible compared to decomposition in the presence of the photocatalyst. The experiments were conducted under UV–Vis light with high UV intensity (UV irradiation) and artificial solar light (ASL) in an air atmosphere. The photocatalytic reaction took place in a glass beaker (0.3 L) containing 0.8 g/L of photocatalyst and 0.2 L of pollutant solution. The starting concentration of the dye was 10 mg/L. Before the irradiation, the suspension was stirred in the dark to ensure the establishment of the adsorption–desorption equilibrium. The adsorption time was determined individually for each contaminant based on the previously performed adsorption tests for the tested photocatalysts (as described

in the previous section). After adsorption, the solution was irradiated using a suitable radiation source. A group of six lamps, each with a power of 20 W (Philips), was used as a UV light (310–430 nm), and the radiation intensity was about 110 W/m² in the range of 280–400 nm and 115 W/m² in the range of 300–2800 nm. A halogen lamp with a power of 60 W (Philips) and intensity of about 0.3 W/m² (measured in the range of 280–400 nm) and 720 W/m² (measured in the range of 300–2800 nm) was used as an artificial solar light source. The photocatalytic decomposition of model organic contaminants under UV irradiation was carried out until their concentration equaled zero. In the case of ASL, the degradation was carried out for 5 h. The concentration of methylene blue in the solutions was measured using a UV–Vis V-630 spectrophotometer (JASCO International Co., LTD., Tokyo, Japan). The degree of MB degradation is presented as C/C_0 , where C is the MB concentration at the irradiation time interval and C_0 is the initial concentration of MB after the adsorption–desorption equilibrium is established. The recycling experiment for one selected sample was undertaken through the degradation of methylene blue over 120 min of irradiation. After each cycle, the material was removed by filtration and dried at 100 °C.

3.6. Reusability Test

The reusability test of the selected photocatalyst was carried out seven times under the same conditions as the photocatalytic test. However, after each cycle, the photocatalyst was separated by filtration, dried at 100 °C, and then added to a new portion of the MB solution.

4. Conclusions

In summary, novel TiO₂/rGO-*t* photocatalysts were obtained in a two-step preparation process. The two preparation steps were connected: a solvothermal method and calcination in an inert gas atmosphere. The calcination process was conducted at 300–900 °C in an argon flow. The presence of rGO in the TiO₂ samples after calcination was confirmed by Raman spectroscopy, SEM, XPS, and elemental analysis. It was found that both rGO modification and the calcination process impacted the crystallite size, the changes in the crystal structure, and the specific surface area of the nanomaterials. It was observed that rGO modification contributed to maintaining a relatively high surface as well as suppressing the phase transition after calcination. The photoactivity of the obtained photocatalysts was tested via the methylene blue decomposition under two types of irradiation: UV and artificial solar light. The influence of adsorption on photoactivity was also investigated. It was found that the photocatalytic activity increased with the modification temperature up to 700 °C. The best result was observed for the TiO₂/rGO-700 photocatalyst, which contained 85% anatase and 15% rutile. Relatively high activity, especially under artificial solar light, was found for samples obtained at 800 and 900 °C due to the redshift edging towards visible light and the narrowing of the band-gap energy. The redshift was caused by the presence of the rutile phase. It was also noted that, in the case of methylene blue degradation, adsorption plays an important role due to π - π interactions between methylene blue molecules and aromatic regions of rGO.

Author Contributions: Conceptualization, A.W.; Funding acquisition, A.W.M.; Investigation, A.W., A.C., and D.M.; Methodology, A.W. and E.K.-N.; Supervision, A.W. and A.W.M.; Writing—Original draft, A.W., A.C., and D.M.; Writing—Review & editing, A.W.M. and E.K.-N. All authors have read and agreed to the published version of the manuscript.

Funding: This study was funded by the National Science Centre (Poland) grant no. DEC-2012/06/A/ST5/00226.

Data Availability Statement: Not applicable.

Conflicts of Interest: The authors have no competing interests to declare.

References

1. Muñoz, I.; Gómez, M.; Molina-Díaz, A.; Huijbregts, M.; Fernández-Alba, A.; García-Calvo, E. Ranking potential impacts of priority and emerging pollutants in urban wastewater through life cycle impact assessment. *Chemosphere* **2008**, *74*, 37–44. [[CrossRef](#)]
2. Wankhade Atul, V.; Gaikwad, G.S.; Dhonde, M.G.; Khaty, N.T.; Thakare, S.R. Removal of organic pollutant from water by heterogeneous photocatalysis: A review. *Res. J. Chem. Environ.* **2013**, *17*, 84–94.
3. Grabowska-Musiał, E.; Marchelek, M.; Klimczuk, T.; Trykowski, G.; Zaleska-Medynska, A. Noble metal modified TiO₂ microspheres: Surface properties and photocatalytic activity under UV-vis and visible light. *J. Mol. Catal. A Chem.* **2016**, *423*, 191–206. [[CrossRef](#)]
4. Khedr, T.M.; El-Sheikh, S.M.; Hakki, A.; Ismail, A.A.; Badawy, W.A.; Bahnmann, D.W. Highly active non-metals doped mixed-phase TiO₂ for photocatalytic oxidation of ibuprofen under visible light. *J. Photochem. Photobiol. A Chem.* **2017**, *346*, 530–540. [[CrossRef](#)]
5. Gupta, S.M.; Tripathi, M. A review of TiO₂ nanoparticles. *Chin. Sci. Bull.* **2011**, *56*, 1639–1657. [[CrossRef](#)]
6. Yun, S.-M.; Palanivelu, K.; Kim, Y.-H.; Kang, P.-H.; Lee, Y.-S. Preparation and characterization of carbon covered TiO₂ using sucrose for solar photodegradation. *J. Ind. Eng. Chem.* **2008**, *14*, 667–671. [[CrossRef](#)]
7. Shao, P.; Tian, J.; Zhao, Z.; Shi, W.; Gao, S.; Cui, F. Amorphous TiO₂ doped with carbon for visible light photodegradation of rhodamine B and 4-chlorophenol. *Appl. Surf. Sci.* **2015**, *324*, 35–43. [[CrossRef](#)]
8. Khalid, N.; Hong, Z.; Ahmed, E.; Zhang, Y.; Chan, H.; Ahmad, M. Synergistic effects of Fe and graphene on photocatalytic activity enhancement of TiO₂ under visible light. *Appl. Surf. Sci.* **2012**, *258*, 5827–5834. [[CrossRef](#)]
9. Rodriguez-Reinoso, F. The role of carbon materials in heterogeneous catalysis. *Carbon* **1998**, *36*, 159–175. [[CrossRef](#)]
10. Leary, R.; Westwood, A. Carbonaceous nanomaterials for the enhancement of TiO₂ photocatalysis. *Carbon* **2011**, *49*, 741–772. [[CrossRef](#)]
11. Low, F.W.; Lai, C.W. Recent developments of graphene-TiO₂ composite nanomaterials as efficient photoelectrodes in dye-sensitized solar cells: A review. *Renew. Sustain. Energy Rev.* **2018**, *82*, 103–125. [[CrossRef](#)]
12. Štengl, V.; Popelková, D.; Vláčil, P. TiO₂-Graphene Nanocomposite as High Performance Photocatalysts. *J. Phys. Chem. C* **2011**, *115*, 25209–25218. [[CrossRef](#)]
13. Bell, N.J.; Ng, Y.H.; Du, A.; Coster, H.; Smith, S.; Amal, R. Understanding the Enhancement in Photoelectrochemical Properties of Photocatalytically Prepared TiO₂-Reduced Graphene Oxide Composite. *J. Phys. Chem. C* **2011**, *115*, 6004–6009. [[CrossRef](#)]
14. Mishra, A.K.; Ramaprabhu, S. Functionalized Graphene-Based Nanocomposites for Supercapacitor Application. *J. Phys. Chem. C* **2011**, *115*, 14006–14013. [[CrossRef](#)]
15. Anjusree, G.S.; Nair, A.S.; Nair, S.V.; Vadukumpully, S. One-pot hydrothermal synthesis of TiO₂/graphene nanocomposites for enhanced visible light photocatalysis and photovoltaics. *RSC Adv.* **2013**, *3*, 12933–12938. [[CrossRef](#)]
16. Yadav, H.M.; Kim, J.-S. Solvothermal synthesis of anatase TiO₂-graphene oxide nanocomposites and their photocatalytic performance. *J. Alloy. Compd.* **2016**, *688*, 123–129. [[CrossRef](#)]
17. Monteagudo, J.; Durán, A.; Martínez, J.M.M.; Martín, I.S. Effect of reduced graphene oxide load into TiO₂ P25 on the generation of reactive oxygen species in a solar photocatalytic reactor. Application to antipyrine degradation. *Chem. Eng. J.* **2019**, *380*, 122410. [[CrossRef](#)]
18. De Oliveira, A.G.; Nascimento, J.P.; Gorgulho, H.D.F.; Martelli, P.; Furtado, C.A.; Figueiredo, J.L. Electrochemical synthesis of TiO₂/Graphene oxide composite films for photocatalytic applications. *J. Alloy. Compd.* **2016**, *654*, 514–522. [[CrossRef](#)]
19. Jiang, G.; Lin, Z.; Chen, C.; Zhu, L.; Chang, Q.; Wang, N.; Wei, W.; Tang, H. TiO₂ nanoparticles assembled on graphene oxide nanosheets with high photocatalytic activity for removal of pollutants. *Carbon* **2011**, *49*, 2693–2701. [[CrossRef](#)]
20. Shanmugam, M.; Alsalmeh, A.; Alghamdi, A.; Jayavel, R. In-situ microwave synthesis of graphene-TiO₂ nanocomposites with enhanced photocatalytic properties for the degradation of organic pollutants. *J. Photochem. Photobiol. B Biol.* **2016**, *163*, 216–223. [[CrossRef](#)]
21. Li, J.; Zhou, S.L.; Hong, G.-B.; Chang, C.-T. Hydrothermal preparation of P25-graphene composite with enhanced adsorption and photocatalytic degradation of dyes. *Chem. Eng. J.* **2013**, *219*, 486–491. [[CrossRef](#)]
22. Liu, Y. Hydrothermal synthesis of TiO₂-RGO composites and their improved photocatalytic activity in visible light. *RSC Adv.* **2014**, *4*, 36040–36045. [[CrossRef](#)]
23. Hu, C.; Chen, F.; Lu, T.; Lian, C.; Zheng, S.; Zhang, R. Aqueous production of TiO₂-graphene nanocomposites by a combination of electrostatic attraction and hydrothermal process. *Mater. Lett.* **2014**, *121*, 209–211. [[CrossRef](#)]
24. Shen, J.; Yan, B.; Shi, M.; Ma, H.; Li, N.; Ye, M. One step hydrothermal synthesis of TiO₂-reduced graphene oxide sheets. *J. Mater. Chem. A* **2011**, *21*, 3415–3421. [[CrossRef](#)]
25. Wang, Y.; Li, Z.; He, Y.; Li, F.; Liu, X.; Yang, J. Low-temperature solvothermal synthesis of graphene-TiO₂ nanocomposite and its photocatalytic activity for dye degradation. *Mater. Lett.* **2014**, *134*, 115–118. [[CrossRef](#)]
26. Kim, M.; Hong, W.H.; Kim, W.; Park, S.H.; Jo, W.K. 2D reduced graphene oxide-titania nanocomposites synthesized under different hydrothermal conditions for treatment of hazardous organic pollutants. *Particuology* **2018**, *36*, 165–173. [[CrossRef](#)]
27. Hu, J.; Li, H.; Muhammad, S.; Wu, Q.; Zhao, Y.; Jiao, Q. Surfactant-assisted hydrothermal synthesis of TiO₂/reduced graphene oxide nanocomposites and their photocatalytic performances. *J. Solid State Chem.* **2017**, *253*, 113–120. [[CrossRef](#)]
28. Torres, S.M.; Pastrana-Martínez, L.M.; Figueiredo, J.; Faria, J.L.; Silva, A. Design of graphene-based TiO₂ photocatalysts—a review. *Environ. Sci. Pollut. Res.* **2012**, *19*, 3676–3687. [[CrossRef](#)] [[PubMed](#)]

29. Carp, O. Photoinduced reactivity of titanium dioxide. *Prog. Solid State Chem.* **2004**, *32*, 33–177. [[CrossRef](#)]
30. Zhang, Y.; Hou, X.; Sun, T.; Zhao, X. Calcination of reduced graphene oxide decorated TiO₂ composites for recovery and reuse in photocatalytic applications. *Ceram. Int.* **2017**, *43*, 1150–1159. [[CrossRef](#)]
31. Nguyen-Phan, T.-D.; Pham, V.H.; Yun, H.; Kim, E.J.; Hur, S.H.; Chung, J.S.; Shin, E.W. Influence of heat treatment on thermally-reduced graphene oxide/TiO₂ composites for photocatalytic applications. *Korean J. Chem. Eng.* **2011**, *28*, 2236–2241. [[CrossRef](#)]
32. Gao, Y.; Pu, X.; Zhang, D.; Ding, G.; Shao, X.; Ma, J. Combustion synthesis of graphene oxide–TiO₂ hybrid materials for photodegradation of methyl orange. *Carbon* **2012**, *50*, 4093–4101. [[CrossRef](#)]
33. Ismail, A.A.; Geioushy, R.; Bouzid, H.; Al-Sayari, S.A.; Al-Hajry, A.; Bahnemann, D.W. TiO₂ decoration of graphene layers for highly efficient photocatalyst: Impact of calcination at different gas atmosphere on photocatalytic efficiency. *Appl. Catal. B Environ.* **2013**, *129*, 62–70. [[CrossRef](#)]
34. Chun, H.-H.; Jo, W.-K. Adsorption and photocatalysis of 2-ethyl-1-hexanol over graphene oxide–TiO₂ hybrids post-treated under various thermal conditions. *Appl. Catal. B Environ.* **2016**, *180*, 740–750. [[CrossRef](#)]
35. Kusiak-Nejman, E.; Wanag, A.; Kozar, J.K.; Kowalczyk, L.; Zgrzebnicki, M.; Tryba, B.; Przepiórski, J.; Morawski, A.W. Methylene blue decomposition on TiO₂/reduced graphene oxide hybrid photocatalysts obtained by a two-step hydrothermal and calcination synthesis. *Catal. Today* **2019**, *357*, 630–637. [[CrossRef](#)]
36. Guskos, N.; Zolnierkiewicz, G.; Gusko, A.; Aidinis, K.; Wanag, A.; Kusiak-Nejman, E.; Narkiewicz, U.; Morawski, A.W. Magnetic moment centers in titanium dioxide photocatalysts loaded on reduced graphene oxide flakes. *Rev. Adv. Mater. Sci.* **2021**, in press.
37. Zhang, W.; Guo, H.; Sun, H.; Zeng, R.-C. Hydrothermal synthesis and photoelectrochemical performance enhancement of TiO₂/graphene composite in photo-generated cathodic protection. *Appl. Surf. Sci.* **2016**, *382*, 128–134. [[CrossRef](#)]
38. Dubey, P.K.; Tripathi, P.; Tiwari, R.; Sinha, A.; Srivastava, O. Synthesis of reduced graphene oxide–TiO₂ nanoparticle composite systems and its application in hydrogen production. *Int. J. Hydrog. Energy* **2014**, *39*, 16282–16292. [[CrossRef](#)]
39. Zhang, Y.; Tang, Z.-R.; Fu, X.; Xu, Y.-J. TiO₂–Graphene Nanocomposites for Gas-Phase Photocatalytic Degradation of Volatile Aromatic Pollutant: Is TiO₂–Graphene Truly Different from Other TiO₂–Carbon Composite Materials? *ACS Nano* **2010**, *4*, 7303–7314. [[CrossRef](#)]
40. Pastrana-Martínez, L.M.; Morales-Torres, S.; Likodimos, V.; Figueiredo, J.; Faria, J.; Falaras, P.; Silva, A. Advanced nanostructured photocatalysts based on reduced graphene oxide–TiO₂ composites for degradation of diphenhydramine pharmaceutical and methyl orange dye. *Appl. Catal. B Environ.* **2012**, *123–124*, 241–256. [[CrossRef](#)]
41. Reyescoronado, D.; Gattorno, G.R.; Espinosa-Pesqueira, M.E.; Cab, C.; De Coss, R.; Oskam, G. Phase-pure TiO₂ nanoparticles: Anatase, brookite and rutile. *Nanotechnology* **2008**, *19*, 145605–145615. [[CrossRef](#)] [[PubMed](#)]
42. Hussain, M.; Russo, N.; Saracco, G. Photocatalytic abatement of VOCs by novel optimized TiO₂ nanoparticles. *Chem. Eng. J.* **2011**, *166*, 138–149. [[CrossRef](#)]
43. Fan, Z.; Wu, T.; Xu, X. Synthesis of Reduced Grapheme Oxide as A Platform for loading β-NaYF₄:Ho³⁺@TiO₂Based on An Advanced Visible Light-Driven Photocatalyst. *Sci. Rep.* **2017**, *7*, 13833. [[CrossRef](#)]
44. Sriwong, C.; Choojun, K.; Tejangkura, W.; Prasansang, W. Preparation and Photocatalytic Activities of TiO₂-rGO Nanocomposite Catalysts for MB Dye Degradation over Sunlight Irradiation. *Mater. Sci. Forum* **2018**, *936*, 47–52. [[CrossRef](#)]
45. Trapalis, A.; Todorova, N.; Giannakopoulou, T.; Boukos, N.; Speliotis, T.; Dimotikali, D.; Yu, J. TiO₂/graphene composite photocatalysts for NO_x removal: A comparison of surfactant-stabilized graphene and reduced graphene oxide. *Appl. Catal. B Environ.* **2016**, *180*, 637–647. [[CrossRef](#)]
46. Rong, X.; Qiu, F.; Zhang, C.; Fu, L.; Wang, Y.; Yang, D. Preparation, characterization and photocatalytic application of TiO₂-graphene photocatalyst under visible light irradiation. *Ceram. Int.* **2015**, *41*, 2502–2511. [[CrossRef](#)]
47. He, Y.; Zhang, Y.; Huang, H.; Zhang, R. Synthesis of titanium dioxide-reduced graphite oxide nanocomposites and their photocatalytic performance. *Micro Nano Lett.* **2013**, *8*, 483–486. [[CrossRef](#)]
48. Yang, Y.; Luo, L.; Xiao, M.; Li, H.; Pan, X.; Jiang, F. One-step hydrothermal synthesis of surface fluorinated TiO₂/reduced graphene oxide nanocomposites for photocatalytic degradation of estrogens. *Mater. Sci. Semicond. Process.* **2015**, *40*, 183–193. [[CrossRef](#)]
49. Tayel, A.; Ramadan, A.R.; El Seoud, O.A. Titanium Dioxide/Graphene and Titanium Dioxide/Graphene Oxide Nanocomposites: Synthesis, Characterization and Photocatalytic Applications for Water Decontamination. *Catalysts* **2018**, *8*, 491. [[CrossRef](#)]
50. Ganguly, A.; Sharma, S.; Papakonstantinou, P.; Hamilton, J. Probing the Thermal Deoxygenation of Graphene Oxide Using High-Resolution In Situ X-ray-Based Spectroscopies. *J. Phys. Chem. C* **2011**, *115*, 17009–17019. [[CrossRef](#)]
51. Park, M.-S.; Kang, M. The preparation of the anatase and rutile forms of Ag–TiO₂ and hydrogen production from methanol/water decomposition. *Mater. Lett.* **2008**, *62*, 183–187. [[CrossRef](#)]
52. Ruidíaz-Martínez, M.; Álvarez, M.A.; López-Ramón, M.V.; Cruz-Quesada, G.; Rivera-Utrilla, J.; Sánchez-Polo, M. Hydrothermal Synthesis of rGO-TiO₂ Composites as High-Performance UV Photocatalysts for Ethylparaben Degradation. *Catalysts* **2020**, *10*, 520. [[CrossRef](#)]
53. Nyamukamba, P.; Tichagwa, L.; Greyling, C. The Influence of Carbon Doping on TiO₂ Nanoparticle Size, Surface Area, Anatase to Rutile Phase Transformation and Photocatalytic Activity. *Mater. Sci. Forum* **2012**, *712*, 49–63. [[CrossRef](#)]
54. Wanag, A.; Kusiak-Nejman, E.; Kowalczyk, L.; Kapica-Kozar, J.; Ohtani, B.; Morawski, A.W. Synthesis and characterization of TiO₂/graphitic carbon nanocomposites with enhanced photocatalytic performance. *Appl. Surf. Sci.* **2018**, *437*, 441–450. [[CrossRef](#)]

55. Sing, K.S.W. Reporting physisorption data for gas/solid systems with special reference to the determination of surface area and porosity (Provisional). *Pure Appl. Chem.* **1982**, *54*, 2201–2218. [CrossRef]
56. Leofanti, G.; Padovan, M.; Tozzola, G.; Venturelli, B. Surface area and pore texture of catalysts. *Catal. Today* **1998**, *41*, 207–219. [CrossRef]
57. Shi, R.; Ren, M.; Li, H.; Zhao, J.; Liu, S.; Li, Z.; Ren, J. Graphene supported Cu nanoparticles as catalysts for the synthesis of dimethyl carbonate: Effect of carbon black intercalation. *Mol. Catal.* **2018**, *445*, 257–268. [CrossRef]
58. Available online: <http://www.nanomaterials.pl/properties> (accessed on 1 October 2021).
59. Coi, H.C.; Jung, Y.M.; Kim, S.B. Size effect in the Raman spectra of TiO₂ nanoparticles. *Vib. Spectrosc.* **2005**, *37*, 33–38. [CrossRef]
60. Ma, H.; Yang, J.; Dai, Y.; Zhang, Y.; Lu, B.; Ma, G. Raman study of phase transformation of TiO₂ rutile single crystal irradiated by infrared femtosecond laser. *Appl. Surf. Sci.* **2007**, *253*, 7497–7500. [CrossRef]
61. Tan, L.-L.; Ong, W.-J.; Chai, S.-P.; Mohamed, A.R. Reduced graphene oxide-TiO₂ nanocomposite as a promising visible-light-active photocatalyst for the conversion of carbon dioxide. *Nanoscale Res. Lett.* **2013**, *8*, 465. [CrossRef]
62. Liang, D.; Cui, C.; Hu, H.; Wang, Y.; Xu, S.; Ying, B.; Li, P.; Lu, B.; Shen, H. One-step hydrothermal synthesis of anatase TiO₂/reduced graphene oxide nanocomposites with enhanced photocatalytic activity. *J. Alloy. Compd.* **2014**, *582*, 236–240. [CrossRef]
63. How, G.T.S.; Pandikumar, A.; Ming, H.N.; Ngee, L.H. Highly exposed {001} facets of titanium dioxide modified with reduced graphene oxide for dopamine sensing. *Sci. Rep.* **2014**, *4*, 5044. [CrossRef] [PubMed]
64. Lambert, T.N.; Chavez, C.A.; Hernandez-Sanchez, B.; Lu, P.; Bell, N.S.; Ambrosini, A.; Friedman, T.; Boyle, T.J.; Wheeler, D.R.; Huber, D. Synthesis and Characterization of Titania–Graphene Nanocomposites. *J. Phys. Chem. C* **2009**, *113*, 19812–19823. [CrossRef]
65. Huang, N.M.; Chang, B.Y.S.; An’Amt, M.N.; Marlinda, A.R.; Norazriena, Y.; Muhamad, M.R.; Harrison, I.; Lim, H.N.; Chia, C.H. Facile hydrothermal preparation of titanium dioxide decorated reduced graphene oxide nanocomposite. *Int. J. Nanomed.* **2012**, *7*, 3379–3387. [CrossRef] [PubMed]
66. Mathews, N.; Morales, E.R.; Cortés-Jacome, M.; Antonio, J.A.T. TiO₂ thin films – Influence of annealing temperature on structural, optical and photocatalytic properties. *Sol. Energy* **2009**, *83*, 1499–1508. [CrossRef]
67. Ma, Y.-J.; Lu, F.; Xiang, B.-X.; Zhao, J.-L.; Ruan, S.-C. Fabrication of TiO₂ thin films with both anatase and rutile structures together using the ion-implantation method. *Opt. Mater. Express* **2018**, *8*, 532–540. [CrossRef]
68. Dolat, D.; Mozia, S.; Wróbel, R.; Moszyński, D.; Ohtani, B.; Guskos, N.; Morawski, A.W. Nitrogen-doped, metal-modified rutile titanium dioxide as photocatalysts for water remediation. *Appl. Catal. B Environ.* **2015**, *162*, 310–318. [CrossRef]
69. Briggs, D.; Grant, J.T. *Surface Analysis by Auger and X-ray Photoelectron Spectroscopy in*; IM publications and Surface Spectra Limited: Manchester, UK, 2003.
70. Wen, Y.; Ding, H.; Shan, Y. Preparation and visible light photocatalytic activity of Ag/TiO₂/graphene nanocomposite. *Nanoscale* **2011**, *3*, 4411–4417. [CrossRef] [PubMed]
71. Wang, S.; Zhu, Z.; Coomes, A.; Haghseresht, F.; Lu, G. The physical and surface chemical characteristics of activated carbons and the adsorption of methylene blue from wastewater. *J. Colloid Interface Sci.* **2005**, *284*, 440–446. [CrossRef]
72. Beegam, M.S.; Ullattil, S.G.; Periyat, P. Selective Solar Photocatalysis by High Temperature Stable Anatase TiO₂. *Sol. Energy* **2018**, *160*, 10–17. [CrossRef]
73. Alvaro, M.; Aprile, C.; Benitez, M.; Carbonell, E.; Garcia, H. Photocatalytic Activity of Structured Mesoporous TiO₂ Materials. *J. Phys. Chem. B* **2006**, *110*, 6661–6665. [CrossRef]
74. Herrmann, J.-M. Heterogeneous photocatalysis: Fundamentals and applications to the removal of various types of aqueous pollutants. *Catal. Today* **1999**, *53*, 115–129. [CrossRef]
75. Zhang, H.; Lv, X.-J.; Li, Y.; Wang, Y.; Li, J. P25-Graphene Composite as a High Performance Photocatalyst. *ACS Nano* **2009**, *4*, 380–386. [CrossRef]
76. Siah, W.R.; Lintang, H.O.; Shamsuddin, M.; Yuliati, L. High photocatalytic activity of mixed anatase-rutile phases on commercial TiO₂ nanoparticles. *IOP Conf. Ser. Mater. Sci. Eng.* **2016**, *107*, 012005. [CrossRef]
77. Ohtani, B.; Ogawa, A.Y.; Nishimoto, S.-I. Photocatalytic Activity of Amorphous–Anatase Mixture of Titanium(IV) Oxide Particles Suspended in Aqueous Solutions. *J. Phys. Chem. B* **1997**, *101*, 3746–3752. [CrossRef]
78. Zhang, Z.; Wang, C.-C.; Zakaria, A.R.; Ying, J. Role of Particle Size in Nanocrystalline TiO₂-Based Photocatalysts. *J. Phys. Chem. B* **1998**, *102*, 10871–10878. [CrossRef]
79. Almquist, C.B.; Biswas, P. Role of Synthesis Method and Particle Size of Nanostructured TiO₂ on Its Photoactivity. *J. Catal.* **2002**, *212*, 145–156. [CrossRef]
80. Janus, M.; Kusiak-Nejman, E.; Choina, J.; Morawski, A.W. Lifetime of Carbon-Modified TiO₂ Photocatalysts Under UV Light Irradiation. *Catal. Lett.* **2009**, *131*, 606–611. [CrossRef]
81. Watanabe, M. Dye-sensitized photocatalyst for effective water splitting catalyst. *Sci. Technol. Adv. Mater.* **2017**, *18*, 705–723. [CrossRef]
82. Kusiak-Nejman, E.; Wanag, A.; Kozar, J.K.; Morawski, A.W. Preparation and characterisation of TiO₂ thermally modified with cyclohexane vapours. *Int. J. Mater. Prod. Technol.* **2016**, *52*, 286–297. [CrossRef]